Conference Proceedings of the Society for Experimental Mechanics Series

Helena Jin · Cesar Sciammarella · Sanichiro Yoshida
Luciano Lamberti *Editors*

Advancement of Optical Methods in Experimental Mechanics, Volume 3

Conference Proceedings of the Society for Experimental Mechanics Series

Springer

Conference Proceedings of the Society for Experimental Mechanics Series

Series Editor
Tom Proulx
Society for Experimental Mechanics, Inc.,
Bethel, CT, USA

For further volumes:
http://www.springer.com/series/8922

Helena Jin • Cesar Sciammarella • Sanichiro Yoshida
Luciano Lamberti
Editors

Advancement of Optical Methods in Experimental Mechanics, Volume 3

Conference Proceedings of the Society for Experimental Mechanics Series

Springer

Editors
Helena Jin
Sandia National Laboratories
Livermore, CA
USA

Cesar Sciammarella
Illinois Institute of Technology
Chicago, IL
USA

Sanichiro Yoshida
Department of Chemistry and Physics
Southeastern Louisiana University
Hammond, LA
USA

Luciano Lamberti
Politecnico Di Bari, Bari
Italy

ISSN 2191-5644 ISSN 2191-5652 (electronic)
ISBN 978-3-319-00767-0 ISBN 978-3-319-00768-7 (eBook)
DOI 10.1007/978-3-319-00768-7
Springer Cham Heidelberg New York Dordrecht London

Library of Congress Control Number: 2011929511

Printed on acid-free paper

Springer is part of Springer Science+Business Media (www.springer.com)

Preface

Advancement of Optical Methods in Experimental Mechanics, Volume 3: Proceedings of the 2013 Annual Conference on Experimental and Applied Mechanics represents one of eight volumes of technical papers presented at the SEM 2013 Annual Conference & Exposition on Experimental and Applied Mechanics organized by the Society for Experimental Mechanics and held in Lombard, IL, June 3–5, 2013. The complete Proceedings also includes volumes on: *Dynamic Behavior of Materials; Challenges in Mechanics of Time-Dependent Materials and Processes in Conventional and Multifunctional Materials; Mechanics of Biological Systems and Materials; MEMS and Nanotechnology; Experimental Mechanics of Composite, Hybrid, and Multifunctional Materials; Fracture and Fatigue; Residual Stress, Thermomechanics & Infrared Imaging, Hybrid Techniques and Inverse Problems*.

Each collection presents early findings from experimental and computational investigations on an important area within Experimental Mechanics, Optical Methods being one of these areas.

With the advancement in imaging instrumentation, lighting resources, computational power, and data storage, optical methods have gained wide applications across the experimental mechanics society during the past decades. These methods have been applied for measurements over a wide range of spatial domains and temporal resolutions. Optical methods have utilized a full range of wavelengths from X-ray to visible lights and infrared. They have been developed not only to make two-dimensional and three-dimensional deformation measurements on the surface, but also to make volumetric measurements throughout the interior of a material body.

Livermore, CA, USA — Helena Jin
Chicago, IL, USA — Cesar Sciammarella
Hammond, LA, USA — Sanichiro Yoshida
Politecnico Di Bari, Bari, Italy — Luciano Lamberti

Contents

Chapter 1
Super-Resolution in Ultrasonic NDE

Shanglei Li, Anish Poudel, and Tsuchin Philip Chu

Abstract This paper discusses the use of an iterative back projection (IBP) super-resolution (SR) image reconstruction technique on the carbon epoxy laminates with simulated porosity defects. In order to first validate and evaluate the application of the proposed method, three artificially simulated delamination defects in carbon epoxy laminates were considered. Based on the preliminary results, it was verified that the contrast signal-to-noise ratio (CNR) of the SR image was higher than the bi-cubic interpolation image. Further, the peak signal-to-noise ratio (PSNR) value of SR result had an average increase of 5.7088 dB compared to the bi-cubic interpolation method. This validates the proposed approach used to generate the reconstructed SR images with image quality similar to the original simulated UT images. After the validation, the UT image reconstruction algorithm was applied to the ultrasonic C-scan amplitude images of a porosity sample. Based on the results, it was demonstrated that the SR image achieved better visual quality with an improved image resolution. It was also demonstrated that this method was capable of detecting the defects with more confidence by recovering the defect outline compared to the LR C-scan image. The defect outline in SR images is more distinct to recognize, allowing post-processing work such as measurement of defect size, shape, and location to be much easier.

Keywords NDE • Ultrasound • Image reconstruction • IBP • Super-resolution

1.1 Introduction

The magnitude of damage detection and prevention in existing infrastructures such as highways, bridges, aircraft, railroads, gas and liquid transmission pipelines, waterways and ports, and buildings are of great importance today. This problem has increased dramatically in the last three decades and is likely to keep increasing. Further, an entire new generation of civil, mechanical, and aerospace structures are being developed that are using composites as their main building blocks. These include commercial and military aircraft, space vehicle panels, composite bridges, and other machines that use composites in some form or another. In order to prevent the occurrence of catastrophic failures, it is imperative to develop an intelligent damage detection technique that is simple, robust, and capable of accurately characterizing the extent and location of existing damage in a composite structure. Ultrasonic testing (UT) is a proven NDE method which is predominantly applied during the inspection of composites [1–9]. The main reasons behind this are its large surface, speed, and non-contact testing capabilities. Industrial applications of ultrasonic imaging technology have grown rapidly in past decades as a practical tool for research, development, and health monitoring. Since typical industry applications involve single transducer signal acquisition and translation, improvements in speed are true cost savers and can open the door for new applications where image capture time is limited. Resolution improvements of ultrasonic images are typically achieved by increasing signal frequency and using focused beams. Frequencies from the kHz to GHz ranges are being employed to generate digital images

S. Li (✉)
Department of Electrical and Computer Engineering, Southern Illinois University Carbondale,
1230 Lincoln Drive, Carbondale, IL 62901, USA
e-mail: shanglei@siu.edu

A. Poudel • T.P. Chu
Department of Mechanical Engineering and Energy Process, Southern Illinois University,
1230 Lincoln Drive, Carbondale, IL 62901, USA

H. Jin et al. (eds.), *Advancement of Optical Methods in Experimental Mechanics, Volume 3*,
Conference Proceedings of the Society for Experimental Mechanics Series,
DOI 10.1007/978-3-319-00768-7_1,

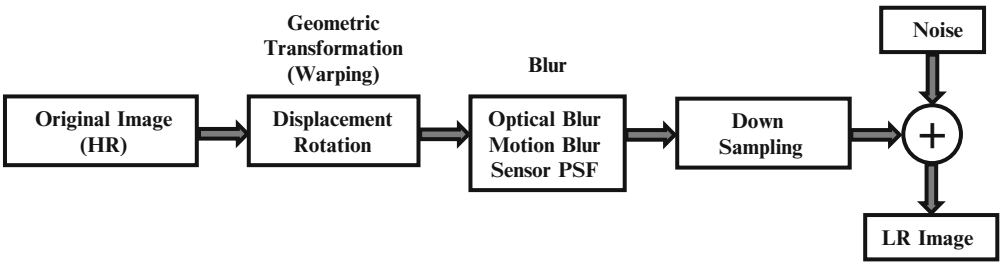

Fig. 1.1 Observation model of the LR image

of regions deep within a material, or at the surface. Details regarding the influences of the focusing lens, pulse frequency, and material properties on the final image resolution have been skillfully reviewed by Gilmore [10]. However, ultrasonic images have lower resolution and poor imaging quality due to the speckle noise produced by the interference of backscattered signals [11–13]. Image data sets obtained from ultrasonic C-scans may not provide satisfactory images for correlation. UT C-scan contrast and detection of defects in composite materials is limited by inhomogeneous density and anisotropic properties of the composites. Moreover, the C-scan image resolution depends on the physical characteristics of ultrasonic transducers (sensor). This makes ultrasonic C-scan inspection difficult to qualitatively and quantitatively evaluate region of interest (ROI). A key NDE goal is to obtain images having the best possible spatiotemporal resolution by limiting the effects of ultrasonic transducers, the uncertainty principles, and the diffraction limits [14]. Super-resolution (SR) image reconstruction is an approach to overcome the inherent resolution limitations of the ultrasonic system. It attempts to solve the problem with software rather than hardware.

This paper discusses an implementation of a SR image reconstruction algorithm based on the lower resolution (LR) image fusion. For this, a micro-scanning imaging technique is utilized to obtain an LR image sequence with sub-pixel displacement. This SR algorithm fuses a set of LR images to form an image with the same resolution as the desired higher resolution (HR) image, and interpolates a LR image as the initialization guess for the iterative restoration algorithm. These images are used to find the HR image by utilizing the iterative back projection (IBP) algorithm.

1.1.1 Super-Resolution Image Reconstruction

Super-resolution image reconstruction is a digital signal processing approach which uses a number of frequency domain aliasing, blurred, and additive noise effect lower resolution images to get high frequency information and more pixel values to overcome the inherent resolution limitations of the existing imaging system. The concept of super-resolution based on a sequential image was firstly introduced by Tsai and Huang [15]. They implemented the frequency domain based approach to reconstruct one improved resolution image from several blurred, down-sampled, and noisy images. After that, various literatures have reported on the use of super-resolution and related topics [16–24].

A typical observation model of the LR image is depicted in Fig. 1.1.

The observed LR image y is assumed to have been deformed during the image acquisition process by geometric transformation (warping), optical blur, motion blur, sensor point spread function (PSF), and downsampling performed on the original HR image X, resulting in a decline in LR image quality. Accordingly, the mathematical model is expressed as:

$$\mathrm{y} = \mathrm{DPRX} + \mathrm{V} \tag{1.1}$$

Where: y is the LR image with resolution of $L_1L_2 \times 1$
D is the downsampling (decimation) matrix $L_1L_2 \times M_1M_2$
P is the blurring matrix of size $M_1M_2 \times M_1M_2$
R is the warping matrix of size $M_1M_2 \times M_1M_2$
X is the original HR image with the size of $M_1M_2 \times 1$
V is the additive noise during the image acquisition process of size $L_1L_2 \times 1$

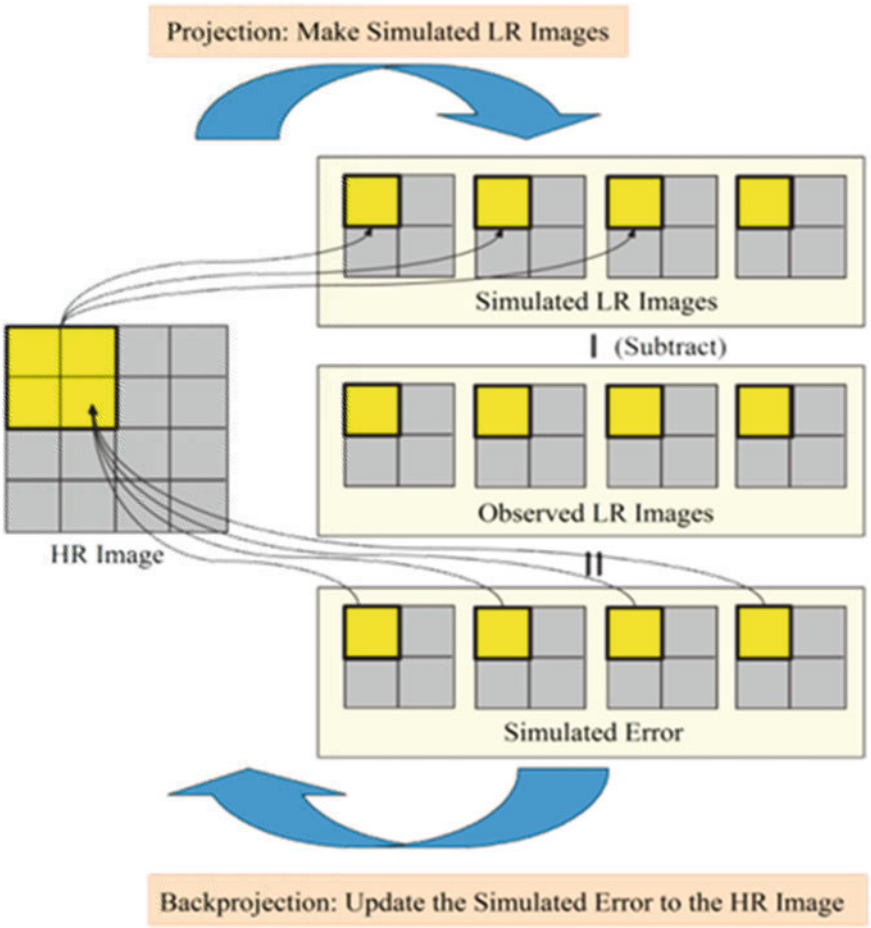

Fig. 1.2 A pictorial example of the IBP method [25]

Thus, the reconstruction of SR image can be considered as solving an ill-posed and ill-conditioned inverse problem that utilizes a set of LR images y_1,y_2,. . .,y_n with a resolution of $L_1 \times L_2$ to solve the HR images $X_1, X_2, \ldots, X_n$ with a resolution of $M_1 \times M_2$.

1.1.2 Iterative Back Projection (IBP) Algorithm

The IBP is a classical algorithm that is based on the back projection technique which is commonly used in computed tomography. This algorithm proposed by Irani and Peleg [17, 18] is based on the idea that the recovered higher resolution (HR) image should produce the same image as the one observed if passing it through the lower resolution (LR) image generation model. The HR image is estimated by back projecting the error (difference) between the simulated LR images and the observed LR images. The process is repeated iteratively until some stopping criteria are met, such as the minimization of the energy of the error or the maximum number of allowed iterations. However, the main limitation of this method is that it usually requires several LR images to recover a high quality HR image. The schematic diagram of IBP method is shown in Fig. 1.2.

1.2 Experimental Setup and Procedure

The material used in this study was a carbon epoxy laminate with simulated porosity defects as shown in Fig. 1.3. This panel had dimensions of 200 × 300 × 3.36 mm. The sample had five simulated porosity defects of varied diameter (15 and 30 mm). These defects were artificially created by controlling the pressure during the curing process. The range of porosity was from 1 % to 5 %.

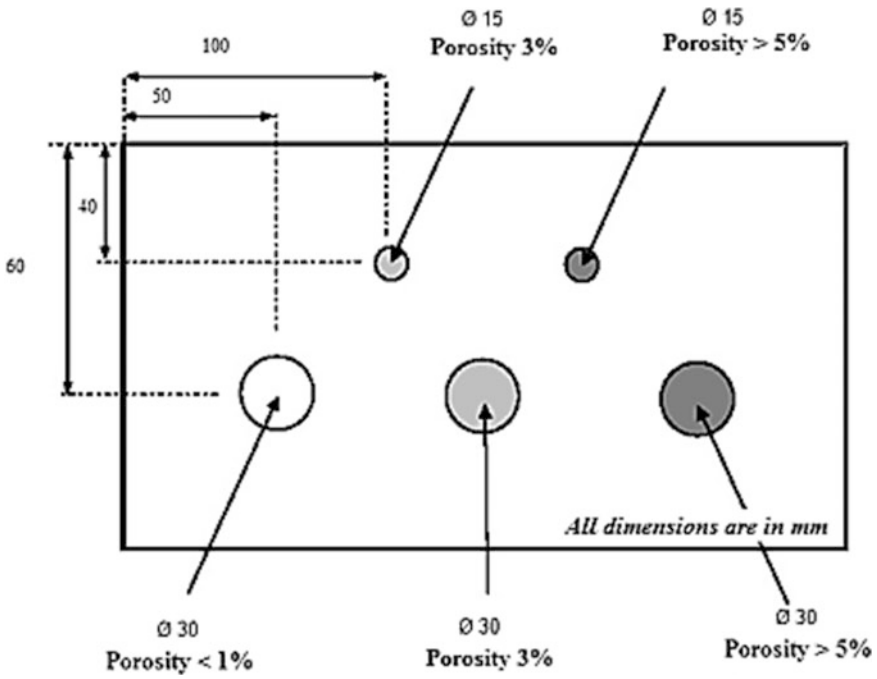

Fig. 1.3 Defect maps in carsimulated porosity defectssimulated porosity defect

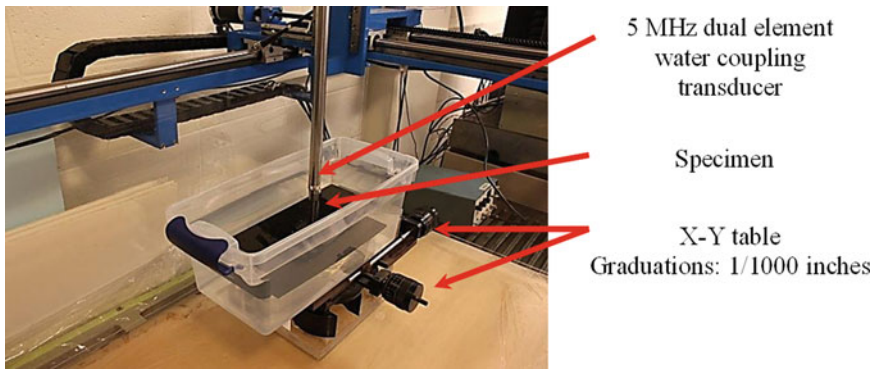

Fig. 1.4 Ultrasonic micro-scanning setup for the carbon epoxy laminates

The pulse-echo ultrasonic C-scans were conducted in an immersion tank using an immersion ultrasonic system as shown in Fig. 1.4. A 5 MHz dual element transducer with a 2 in. focal length was driven by a Panametric 5,072 pulser/receiver. The UT scan increment was 0.01 in.. In pulse-echo (reflection) mode, the transducer performs both the transmitting and the receiving of the pulsed waves as the ultrasonic wave is reflected back to the device. The measured ultrasound is reflected from material interfaces, such as the back wall of the object or from an imperfection within the object. The C-scan machine displays these results in the form of a signal with amplitude representing the intensity of the reflection, and the distance representing the arrival time of the reflection. The micro-scanning method is utilized to obtain multiple sub-pixel displacement LR UT images for the optimum performance of the UT image resolution. This approach is similar to that described in our outside work [26]. For this study, a micro-scanning technique was employed by setting the displacement of 0.003 in. Figure 1.4 depicts an X-Y table with micro-scanning technique to obtain the sub-pixel displacement. The graduation of the X-Y table is 1/1,000 in..

1.3 Results

In order to first validate and evaluate the application of super-resolution UT image reconstruction, three artificially simulated delamination defects were considered. These defect images were generated from ultrasonic 3D data to simulate delaminations in a carbon epoxy laminate. Details on the method used to generate these images are described in our

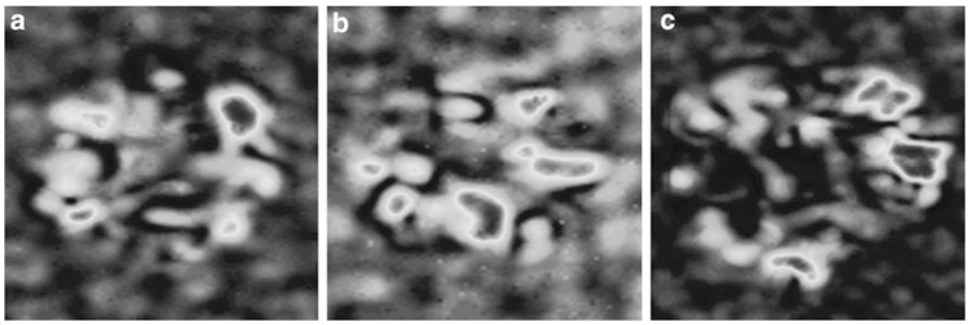

Fig. 1.5 Simulated UT delamination defects (**a**) Defect I, 456 × 432 pixels (**b**) Defect II, 464 × 396 pixels (**c**) Defect III, 508 × 492 pixels

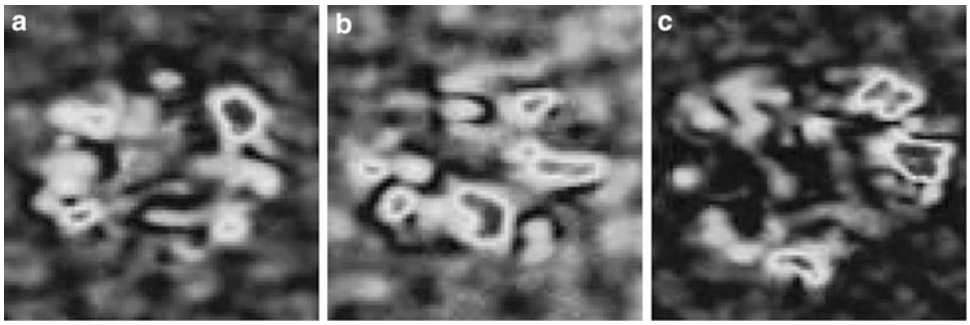

Fig. 1.6 One of the generated subsampled images for each defect (**a**) Defect I, 114 × 108 pixels (**b**) Defect II, 116 × 99 pixels (**c**) Defect III, 127 × 123 pixels

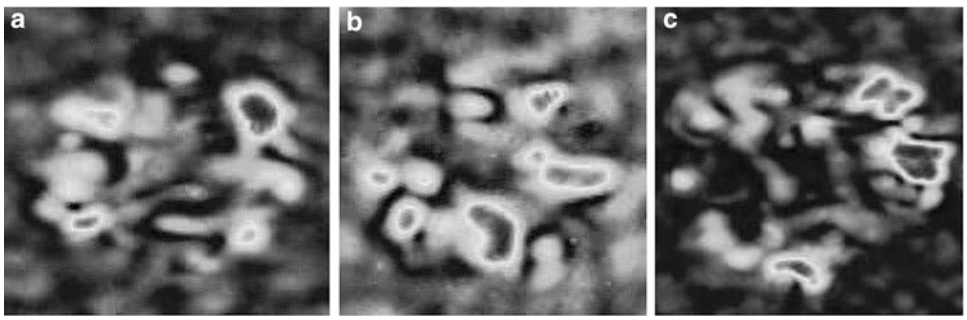

Fig. 1.7 Reconstructed SR image from 9 LR images (**a**) Defect I, 456 × 432 pixels (**b**) Defect II, 464 × 396 pixels (**c**) Defect III, 508 × 492 pixels

outside work [24]. The test images were 456 × 432, 464 × 396, and 508 × 492 pixels, and plotted in 8 bit grayscale images (256 Gy levels) as shown in Fig. 1.5.

In order to simulate the LR image sets obtained with micro-scanning technique, each defect image (shown in Fig. 1.5) was subsampled to 16 LR images with resolutions 114 × 108, 116 × 99, and 127 × 123 pixels for defects I, II, and III respectively. Considering the performance of the super-resolution reconstruction and the computational complexity, the best balance was found using 9 LR images for the super-resolution image reconstruction. Thus for this study, 9 of 16 subsampled LR images for each defect are used for SR image reconstruction. For each defect, one of the generated subsampled images is shown in Fig. 1.6. These subsampled images are scaled to the same size as the simulated UT images only for the purposes of displaying and comparing detail.

Then, the IBP SR method was applied to the subsampled LR images. Figure 1.7 shows the reconstructed SR images from 9 LR images for each type of defects as described earlier. The reconstructed SR image resolution were 456 × 432, 464 × 396, and 508 × 492 pixels for defects I, II, and III respectively.

Table 1.1 Experimental comparison of CNR & PSNR

		CNR (dB)	PSNR (dB)
Defect I	*Bi-cubic interpolation*	0.9515	19.4450
	IBP SR reconstruction	1.1027	23.9556
Defect II	*Bi-cubic interpolation*	0.5907	18.3682
	IBP SR reconstruction	0.6133	24.2702
Defect III	*Bi-cubic interpolation*	1.8549	24.8207
	IBP SR reconstruction	1.9799	29.8042

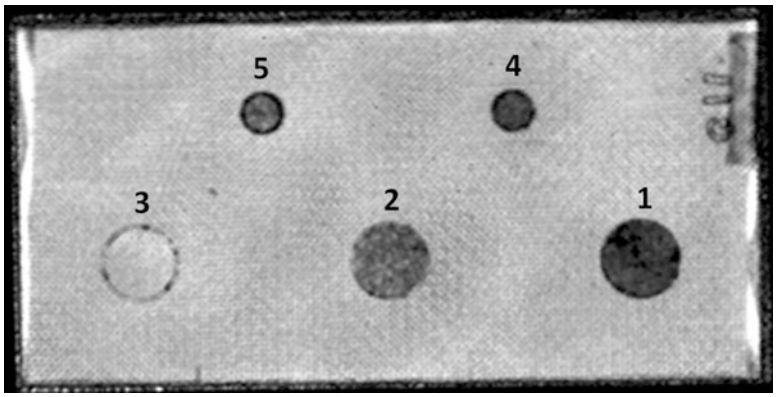

Fig. 1.8 Pulse-echo amplitude C-scan image for carbon epoxy laminates with simulated porosity defects

For subjective evaluation, the subsampled images (shown in Fig. 1.6) were used to reconstruct SR images (as shown in Fig. 1.7) with four times the resolution of the individual subsampled images. Pixel blocking effects were evident from images in Fig. 1.6 due to the low spatial resolution. In contrast, SR images (shown in Fig. 1.7) had smoother and clearer edges than the studied subsampled images.

Furthermore, to test the reconstructed image quality and robustness of the IBP method, the SR result and bi-cubic interpolation result were compared with the original simulated UT image results respectively. For this, peak signal-to-noise ratio (PSNR) and contrast signal-to-noise ratio (CNR) were employed for quantitative assessment.

The PSNR is given as:

$$PSNR = 10 \cdot \log_{10}\left(\frac{{MAX_I}^2}{MSE}\right) \tag{1.2}$$

Where: MAX_I is the maximum possible pixel value of the image. In this study, all pixels are represented using 8 bits gray level, here MAX_I is 255.

MSE is the mean squared error between two compared images.

The CNR is given as:

$$CNR = \frac{S_i - S_o}{\sqrt{\sigma_i^2 + \sigma_o^2}} \tag{1.3}$$

Where: S_i and S_o are the mean values inside and outside the ROI respectively

σ_i and σ_o are the standard deviations respectively

From Table 1.1, it can be verified that the CNR of the SR image is higher than bi-cubic interpolation image. Further, note that the PSNR value of SR result has an average increase of 5.7088 dB compared to bi-cubic interpolation method. The IBP method provides better performance in PSNR, indicating the quality of the reconstructed SR image is close to the original simulated UT image, which can verify that the IBP method is robust and reliable. Since the proposed method provides good performance in both of CNR and PSNR, we can see that the proposed super-resolution reconstruction method is effective in resolution enhancement.

After the validation procedure, the IBP method was applied on the ultrasonic C-scan images obtained by micro-scanning technique for carbon epoxy laminate with simulated porosity defects. Figure 1.8 shows the 5 MHz ultrasonic pulse-echo

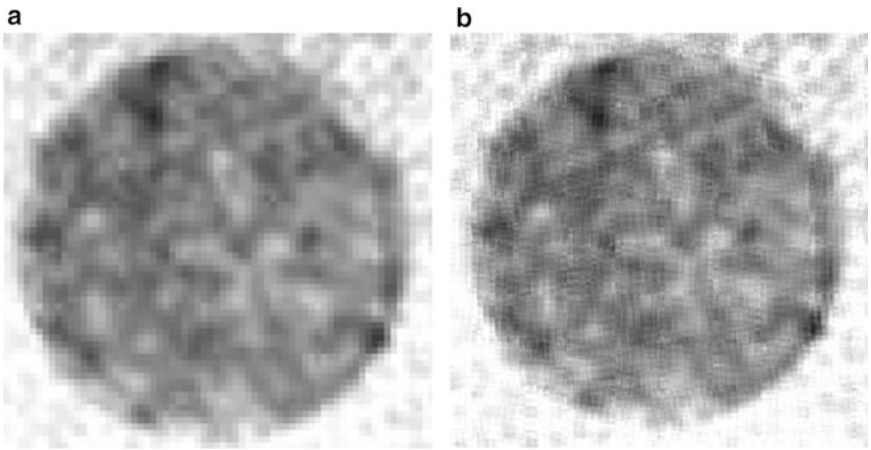

Fig. 1.9 Comparison of micro-scan UT image and SR result images (**a**) One of the micro-scan UT images (**b**) Reconstructed SR image

amplitude C-scan results for carbon epoxy laminates with porosity defects. As shown in Fig. 1.8, the ultrasonic imaging resolution capability becomes poorer for the lower percentage of the porosity. Therefore, super-resolution imaging can be a great tool for resolution improvement to detect lower percentage porosity.

To demonstrate the feasibility of implementing the IBP method on porosity samples, ultrasonic C-scan image (back wall amplitude data) obtained for defect two was considered. The C-scan image for defect two is normalized and plotted in 8 bit grayscale images (256 Gy levels) as shown in Fig. 1.9a, where defect areas are represented by dark shade of gray, i.e. a significant drop in pulse-echo signal amplitude.

Image in Fig. 1.9a is one of the nine images obtained by the micro-scanninchesmethod with the displacement of 0.003 in., approximately 1/3 pixel of the UT image. The resolution of the obtained UT images is 180×180 pixels. For the pre-processing, a 3×3 Wiener filter is applied on UT images to reduce the noise. From the super-resolution results obtained in Fig. 1.9b, comparison indicates that SR image shows better visual quality. The reconstructed SR image's resolution is 720×720 pixels, and it has the capability of detecting defects with more confidence by recovering the defect outline which is not as clear in the LR C-scan image. The defect outline in SR images is more distinctly recognizable, allowing post-processing work such as the measurement of defect size, shape, and location to be much easier.

1.4 Conclusions

The iterative back projection (IBP) super-resolution ultrasonic image reconstruction algorithm was applied to the 5 MHz ultrasonic pulse-echo amplitude C-scan results for carbon epoxy laminates with simulated porosity defects. The experimental results obtained have demonstrated the effectiveness of the applied method. Super-resolution image reconstruction can be utilized to overcome the inherent limitations of the existing ultrasonic C-scan system. For the future work, since the C-scan time is proportional to the desired resolution, to double the resolution in both x and y direction, four times the original scanning time may be required. If a C-scan system is equipped multiple ultrasound transducers with known displacement from each other, the system can offer a SR result with a resolution four times larger than the original UT image while maintaining the same scanning time; or the same resolution image can be achieved with a quarter of the original time.

References

1. Li S, Poudel A, Chu TP (2012) An image enhancement method for ultrasonic NDE of CFRP panels. In: 21st annual research symposium and spring conference, ASNT, Dallas, 19–23 Mar 2012
2. Poudel A, Chu TP, Filip P (2012) Application of ultrasonic non-destructive evaluation in braking materials. In: Proceeding SAE annual brake colloquium, 30th, Society of Automotive Engineers, San Diego
3. Poudel A, Chu TP (2012) Intelligent nondestructive testing expert system for aircraft carbon/carbon composite brakes using infrared thermography and air-coupled ultrasound. Mater Eval 70(10):1219–1229

4. Poudel A, Lane M, Li S, Chu TP (2012) NDE of commercial C/C brake disks standards using air-coupled ultrasonic testing. In: Proceeding nondestructive evaluation of aerospace materials and structures III, St. Louis
5. Chakrapani SK, Dayal V, Hsu DK, Barnard DJ, Gross A (2011) Characterization of waviness in wind turbine blades using air-coupled ultrasonics. In: Thompson DOCDE (ed) Review of progress in quantitative nondestructive evaluation, Vols 30a and 30b, San Diego, pp 956–962. http://proceedings.aip.org/resource/2/apcpcs/1335/1/956_1
6. Hsu DK, Hughes MS (1992) Simultaneous ultrasonic velocity and sample thickness measurement and application in composites. J Acoust Soc Am 92(2):669–675
7. Jeong H, Hsu DK (1995) Experimental analysis of porosity-induced ultrasonic attenuation and velocity change in carbon composites. Ultrasonics 33(3):195–203
8. Livings RA, Dayal V, Barnard DJ, Hsu DK Flaw detection in a multi-material multi-layered composite: using FEM and air-coupled UT. In: Proceeding 37th annual review of progress in quantitative nondestructive evaluation (QNDE), San Diego, pp 942–949. http://proceedings.aip.org/resource/2/apcpcs/1335/1/956_1
9. Nair SM, Hsu DK, Rose JH (1989) Porosity estimation using the frequency dependence of the ultrasonic attenuation. J Nondestruct Eval 8 (1):13–26
10. Gilmore RS (1996) Industrial ultrasonic imaging and microscopy. J Phys D Appl Phys 29(6):1389–1417
11. Hong SK, Ohr YG (1998) Ultrasonic speckle pattern correlation interferometry using a pulse-echo method. J Phys D Appl Phys 31(11):1392–1396
12. HongMei Z, MingXi W, JinJin W, XuLei Q (2010) Super-resolution reconstruction of deformable tissue from temporal sequence of ultrasound images. In: 2010 International conference on artificial intelligence and computational intelligence (AICI 2010), vol 1,Sanya, pp 337–342. http://ieeexplore.ieee.org/xpls/abs_all.jsp?arnumber=5656514&tag=1
13. Kouame D, Ploquin M (2009) Super-resolution in medical imaging: an illustrative approach through ultrasound. In: 2009 IEEE international symposium on biomedical imaging: from Nano to Macro, vols 1 and 2, Boston, pp 249–252. http://ieeexplore.ieee.org/xpls/abs_all.jsp?arnumber=5193030
14. Clark G, Jackson J (2006) Super-resolution algorithms for ultrasonic nondestructive evaluation imagery. J Acoust Soc Am 120(5):3140–3140
15. Tsai RY, Huang TS (1984) Multiframe image restoration and registration. Adv Comput Vis Image Process 1:101–106
16. Stark H, Oskoui P (1989) High resolution image recovery from image plane arrays, using convex projections. J Opt Soc Am A Opt Image Sci Vis 6(11):1715–1726
17. Irani M, Peleg S (1990) Super resolution from image sequences. In: Proceedings 10th international conference on pattern recognition (Cat. No.90CH2898-5), vol 112, Atlantic City, pp 115–120. http://ieeexplore.ieee.org/xpl/articleDetails.jsp?arnumber=479905
18. Irani M, Peleg S (1991) Improving resolution by image registration. CVGIP-Graph Models Image Process 53(3):231–239
19. Schultz RR, Stevenson RL (1995) Improved definition video frame enhancement. In: 1995 international conference on acoustics, speech, and signal processing – conference proceedings, vols 1–5, Detroit, pp 2169–2172
20. Schultz RR, Stevenson RL (1995) Video resolution enhancement. In: Technol, E. Soc Photo Opt Instrumentat (eds) Proceeding conference on image and video processing III, San Jonse, pp 23–34
21. Schultz RR, Stevenson RL (1996) Extraction of high-resolution frames from video sequences. IEEE Trans Image Process 5(6):996–1011
22. Schultz RR, Stevenson RL (1996) Motion-compensated scan conversion of interlaced video sequences. In: Technol, E. Soc Photo Opt Instrumentat (eds) Proceeding conference on image and video processing IV, San Jose, pp 107–118. http://proceedings.spiedigitallibrary.org/proceeding.aspx?articleid=1014864
23. Kang MG, Chaudhuri S (2003) Super-resolution image reconstruction. IEEE Signal Process Mag 20(3):19–20
24. Li S, Chu TP (2012) Ultrasonic 3D reconstruction of CFRP panel delamination. In: ASNT fall conference, ASNT, Orlando, 29 Oct–1 Nov 2012
25. Park SC, Park MK, Kang MG (2003) Super-resolution image reconstruction: a technical overview. IEEE Signal Process Mag 20(3):21–36
26. Li S, Poudel A, Chu TP (2013) Super-resolution image reconstruction for ultrasonic NDE of carbon composites. In: Accepted for proceedings of 22nd annual research symposium and spring conference, Memphis, 18–21 Mar 2013

Chapter 2
Nanoparticle and Collagen Concentration Measurements Using Scanned Laser Pico-projection

Chin-Ho Chuang, Ti-Wen Sung, Chih-Ling Huang, and Yu-Lung Lo

Abstract The images projected by scanned laser pico-projectors (SLPPs) contain speckle noise caused by the reflection of the high coherent laser light source from the projection screen. A speckle pattern can be used to detect the concentration of liquid solution with nanoparticle. Three samples: solid solution, liquid solution, and collagen solution are tested. The experimental results show that the green laser within the SLPP provides a better sensitivity and resolution than the red or blue lasers. In solid solution measurement, different concentrations of nanoparticles embedded in a poly (methyl methacrylate) (PMMA) matrix are tested. In liquid solution measurement, different concentrations of nanoparticles dissolved in deionized water are also tested. Finally, the system shows ability to measure the collagen concentrations from 0.125 % to 0.025 %. Accordingly, the proposed system provides a viable, low-cost solution for high-sensitivity in biomedical, chemical and environmental applications.

Keywords Nanoparticle concentration • Speckle • Scanned laser pico-projector • Collagen

2.1 Introduction

Scanned laser pico-projectors (SLPPs) are an emerging solution for projecting large-scale images using compact portable devices such as notebooks or cell phones. SLPPs comprise red/green/blue laser, each with a lens near the laser output which collects the light from the laser and provides a collimated beam. The projected image is created by modulating the three lasers synchronously with the position of the scanned beam [1]. SLPPs have lots of important practical benefits, including an inherently high image contrast and an infinite focus [1, 2]. Various methods have been proposed for measuring volume roughness directly by means of an ultrafast pulsed laser [3, 4] or the third-order laser speckle frequency correlations of a tunable laser [4, 5] in solid solution. However, these methods are costly and complex. Recently, Curry et al. [6] proposed a study to directly determine diffusion properties of random media from speckle contrast by using a femtosecond pulse laser with controlled bandwidth. In addition, UV/VIS/NIR spectrometers use the Beer-Lambert law to measure the absorbing molecular concentration. However, this method has some limitations that the absorbing medium needs to be homogenous and does not scatter the radiation [7]. Accordingly, the present study exploits the inherent speckle noise characteristics to realize a simple yet highly precise relative nanoparticle concentration measurement in both solid and liquid solutions by only a commercial SLPP device and a digital camera. Finally, it demonstrates the concentration measurements of collagen witch is an important role in the biomedical field, particularly for wound healing, controlled drug delivery and tissue regeneration [8].

C.-H. Chuang • T.-W. Sung • C.-L. Huang • Y.-L. Lo (✉)
Department of Mechanical Engineering, National Cheng Kung University, Tainan 701, Taiwan
e-mail: loyl@mail.ncku.edu.tw

H. Jin et al. (eds.), *Advancement of Optical Methods in Experimental Mechanics, Volume 3*,
Conference Proceedings of the Society for Experimental Mechanics Series,
DOI 10.1007/978-3-319-00768-7_2,

2.2 Experimental Setup and Nanoparticle Solution Preparation

In the present study, the measurement system was constructed using a commercial SLPP purchased from MicroVision. Four different projection images were created using the red laser, green laser, blue laser, and white light (all lasers on) within the SLPP, respectively. Silica nanoparticles were synthesized by hydrolysis and condensation of TEOS in an ethanol and ammonia by a modified Stöber method [9]. PMMA composite samples containing silica nanoparticles in various concentrations were prepared for solid solution using an in situ polymerization method. The resulting solution was homogeneous, without any phase separation or precipitation. Silica nanoparticles were then added to the PMMA solution in concentrations of 0, 1, 2, 3, 4 and 5 wt%, respectively. The PMMA/silica nanoparticle solutions were dripped onto a Teflon sheet and left to dry under ambient conditions. Following the evaporation of the toluene content, polymeric composite sheets of PMMA/silica nanoparticles with a thickness of approximately 2 mm were obtained.

In liquid solution, the silica nanoparticles were dissolved in deionized water at six different concentrations (0, 0.001, 0.002, 0.003, 0.004 and 0.005 M). The resulting solution was homogeneous without phase separation or precipitation. Subsequently, the nanoparticle solution was put into a quartz cuvette for further experiments (Fig. 2.1).

2.3 Concentration Measurements

2.3.1 Measurement in Solid Solution

Figure 2.2 shows the experimental results obtained for the variation of the speckle contrast with the nanoparticle concentration given green/red/blue/white (all lasers on) illumination light, respectively. It is seen that for a given nanoparticle concentration, the green image has a greater speckle contrast than the red or blue images. Consequently, the green laser is better suited to volume roughness measurement than the red or blue lasers. Figure 2.2 shows that the maximum sensitivity of the measurement system is equal to −8.59 ((speckle contrast %)/(wt%)). The average standard deviation of the speckle contrast in the green image over three repeated experiments was found to be 0.11 (speckle contrast %). Thus, the resolution of the measurement system (using the green image) was determined to be 0.013 (wt%).

2.3.2 Measurement in Liquild Solution

Figure 2.3 shows the experimental results obtained for the variation of the speckle contrast with the nanoparticle concentration given green/red/blue/white illumination light, respectively. It is seen that for a given nanoparticle concentration, the green image has a greater speckle contrast than the red or blue images as observed in solid solution measurement.

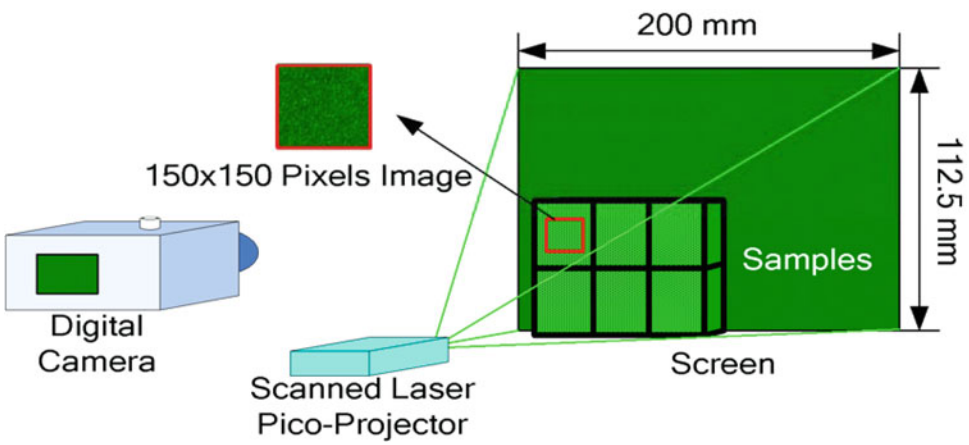

Fig. 2.1 Experimental setup of nanoparticle concentration measurement [10]

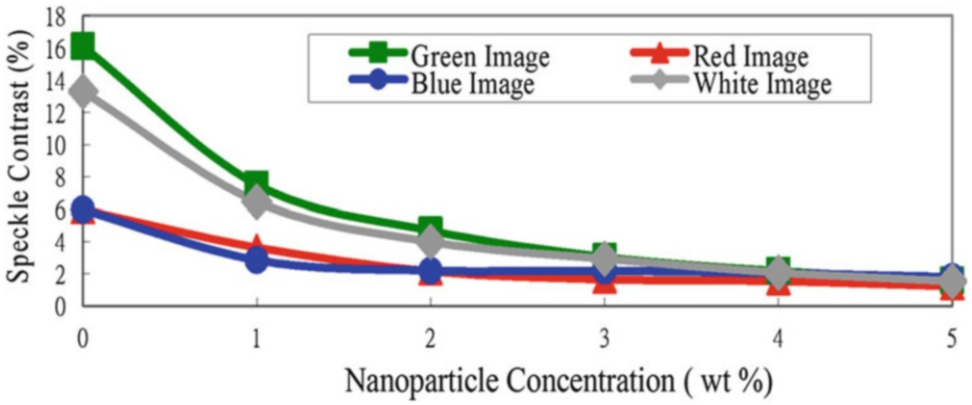

Fig. 2.2 Speckle contrast versus nanoparticle concentration in PMMA matrix

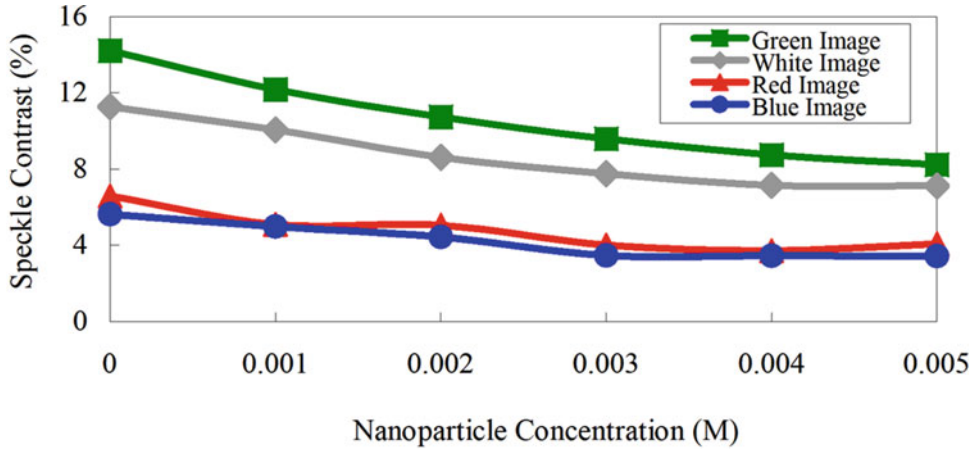

Fig. 2.3 Speckle contrast with nanoparticle concentration

However, the green image speckle contrast of a quartz cuvette with 0 M nanoparticle concentration is about 14.22 %. Figure 2.3 shows that the maximum sensitivity with green image is equal to −2050 (speckle contrast %/M). The resolution of the measurement system (using the green image) was determined to be 7.51×10^{-5} M.

2.3.3 Measurement in Collagen Solution

Collagen from calf skin (Sigma C9719) was dissolved in 0.1 M acetic acid solution (Fluka) under moderate magnetic stirring for 3 h at room temperature. The resulting solution was homogeneous, without any phase separation or precipitation. Collagen powder was prepared as a 0.5 % collagen type I solution in 0.1 M acetic acid (i.e., 5 mg collagen/1 ml 0.1 M acetic acid) and diluted in concentrations of 0.125, 0.100, 0.075, 0.050 and 0.025 wt%, respectively. Subsequently, the collagen type I solution was put into a quartz cuvette for further experiments. Figure 2.4 shows the experimental results obtained for the variation of the speckle contrast with the collagen concentration given green illumination light. It shows that the biomaterial concentration is successfully demonstrated.

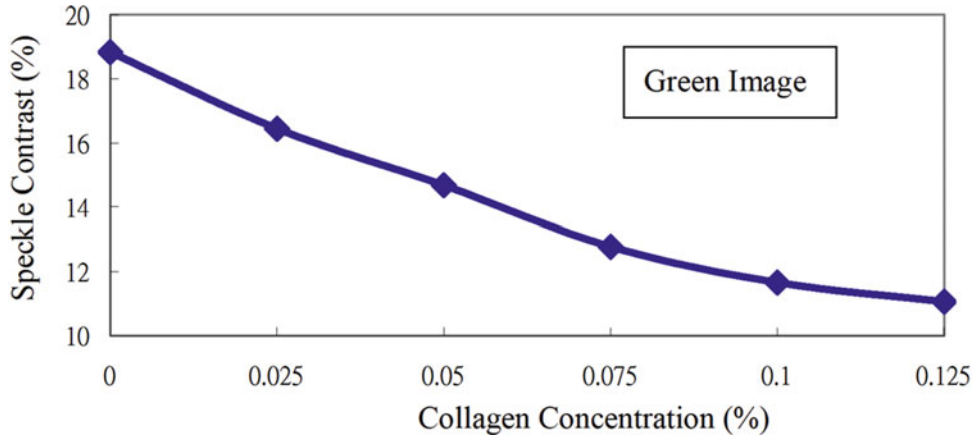

Fig. 2.4 Speckle contrast with collagen concentration under green light illumination

2.4 Conclusions

The experimental results have shown that a higher sensitivity and resolution are obtained when the sample is illuminated using the green laser within the SLPP. As a result, it provides an effective tool for a variety of nanoparticle concentration measurements in solid and liquid solutions, and the new expectations including biomedical, chemical and environmental applications can be explored. The collagen concentration measurement is an important demonstration in this study.

Acknowledgements The financial support provided to this study by the National Science Council of Taiwan, R.O.C., under contract no. NSC 99-2221-E-006-034-MY3 is gratefully acknowledged. This work has been partially published in Chuang C-H et al. (2012) Relative two-dimensional nanoparticle concentration measurement based on scanned laser pico-projection. *Sensors and Actuators B: Chemical* **173**: 281–287.

References

1. Freeman M, Champion M, Madhavan S (2009) Scanned laser pico-projectors: seeing the big picture (with a small device). Opt Photonic News 20:28–34
2. Chellappan KV, Erden E, Urey H (2010) Laser-based displays: a review. Appl Opt 49:F79–F97
3. Riechert F, Glockler F, Lemmer U (2009) Method to determine the speckle characteristics of front projection screens. Appl Opt 48:1316–1321
4. Webster MA, Webb KJ, Weiner AM (2003) Temporal response of a random medium from speckle intensity frequency correlations. J Opt Soc Am A 20:2057–2069
5. Webster MA, Webb KJ, Weiner AM (2002) Temporal response of a random medium from third-order laser speckle frequency correlations. Phys Rev Lett 88:033901
6. Churry N, Bondareff P, Leclercq M, van Hulst NF, Sapienza R, Gigan S, Gresillon S (2011) Direct determination of diffusion properties of random media from speckle contrast. Opt Lett 36:3332–3334
7. Ingle JDJ, Crouch SR (1988) Spectrochemical analysis. Prentice Hall, New Jersey
8. Wolfgang F (1998) Collagen–biomaterial for drug delivery. Eur J Pharm Biopharm 45:113–136
9. Stöber W, Fink A, Bohn E (1968) Controlled growth of monodisperse silica spheres in the micron size range. J Colloid Interface Sci 26:62–69
10. Chuang C-H, Sung T-W, Huang C-L, Lo Y-L (2012) Relative two-dimensional nanoparticle concentration measurement based on scanned laser pico-projection. Sensors and Actuators B: Chemical 173:281–287

Chapter 3
High-speed Shape Measurement with 4 kHz Using Linear LED Device

Motoharu Fujigaki, Yohei Oura, Daisuke Asai, and Yorinobu Murata

Abstract High-speed shape measurement is required to analysis the behavior of a breaking object, a vibrating object or a rotating object. A shape measurement by a phase shifting method can measure the shape with high spatial resolution because the coordinates can be obtained pixel by pixel. A light source stepping method (LSSM) using linear LED array was proposed by authors. Accurate shape measurement can be performed by a whole space tabulation method (WSTM). The response speed of the LED array is more than 12 kHz. In this paper, high-speed shape measurement is performed with a high-speed camera by WSTM and LSSM using a linear LED array. The phase shifting is performed in 12,000 Hz and the shape measurement of a rotating fan is performed in 4,000 Hz.

Keywords High-speed shape measurement • Linear LED device • Light source stepping method • Whole space tabulation method • Phase shifting method

3.1 Introduction

Accurate 3D shape measurement is requested in industry. High-speed shape measurement is also required to analyze the behavior of a breaking object, a vibrating object or a rotating object. A shape measurement by a phase shifting method can measure the shape with high spatial resolution because the coordinates can be obtained pixel by pixel.

This method needs phase shifting mechanism in the projector as a primary function. High stability, high brightness, high-speed response and low cost are required for a projector for shape measurement. In conventional method, a mechanical grating panel movement method [1, 2], an LCD (liquid crystal display) projector [3, 4] and a DLP (digital light processing) projector using DMD (digital micro-mirror device) [5–7], a MEMS (microelectromechanical system) scanner grating projector [8, 9], and a projector with a free-form mirror [10] are employed to project phase-shifted grating patterns. Especially, high-speed shape measurement was performed using a DLP projector [6, 7].

Authors proposed a light source stepping method (LSSM) using linear LED array [11, 12]. The basic idea was also mentioned in a patent description around 10 years ago [13]. The shape measurement using this idea was not apparently realized at that time. The disadvantage of LSSM is that shifted phase varies according to the z position. However, as the z coordinate and the obtained phase using an algorithm of a phase-shifting method have a one-to-one relationship, accurate shape measurement can be realized using a whole space tabulation method (WSTM) proposed by authors [14, 15]. The shape measurement equipment can be produced with low-cost and compact without any phase-shifting mechanical systems by using this method. Also it enables us to measure 3D shape in very short time by switching the light sources quickly.

M. Fujigaki (✉) • Y. Murata
Department of Opto-Mechatoronics, Wakayama University, 930, Sakaedani, Wakayama 640-8510, Japan
e-mail: fujigaki@sys.wakayama-u.ac.jp

Y. Oura
Graduate School of Systems Engineering, Wakayama University, 930, Sakaedani, Wakayama 640-8510, Japan

D. Asai
HIKARI Co., Ltd., 418-4 Minaminoda, Tohon, Ehime 791-0297, Japan

H. Jin et al. (eds.), *Advancement of Optical Methods in Experimental Mechanics, Volume 3*,
Conference Proceedings of the Society for Experimental Mechanics Series,
DOI 10.1007/978-3-319-00768-7_3,

In this paper, the response speed of the linear LED array produced by authors is verified and high-speed shape measurement is realized. The LSSM with the linear LED array and the WSTM are applied to the high-speed shape measurement with a high-speed camera. The experimental trial to measure the height distribution of a rotating fan in 4,000 Hz with shifting phase in 12,000 Hz is performed.

3.2 Principle

3.2.1 Light Source Stepping Method (LSSM)

Figure 3.1 shows a schematic illustration of projected grating pattern with a point light source and a grating plate such as a Ronchi ruling. A grating plate is placed between a light source and an object. When the light source is assumed to be a point light source, the shadow of the grating plate is projected on the object. As shown in this figure, the projected phase $\phi(x_p, z_p)$ at point P(x_p, z_p) on the object becomes the same phase at point G(x_g, z_g) on the grating plate. Point G is a intersection of a line connecting the point of light source S(x_s, z_s) and point P with the grating plate.

The phase ϕ on the grating plate is expressed in Eq. 3.1,

$$\phi(x, z_g) = \frac{2\pi x}{p} + \phi_0, \tag{3.1}$$

where p is a pitch of the grating and ϕ_0 is an intercept value at $x = 0$. The x coordinate at point G is calculated from the coordinates of point S and point P as shown in Eq. 3.2,

$$x_g = \frac{x_p - x_s}{z_p - z_s}(z_g - z_s) + x_s = \frac{z_g - z_s}{z_p - z_s}x_p + \frac{z_p - z_g}{z_p - z_s}x_s. \tag{3.2}$$

The projected phase $\phi(x_p, z_p)$ at point P is obtained as shown in Eq. 3.3,

$$\phi(x_p, z_p) = \phi(x_g, z_g) = \frac{2\pi x_g}{p} + \phi_0. \tag{3.3}$$

Figure 3.2 shows a schematic illustration of phase-shifted projected grating patterns using a light source stepping method. The projected grating pattern is changed with stepping the light source position as shown in Fig. 3.2. The projected phase at point P on an object is also changed according to the position of the light source. When the position of light source is stepped from S to S′ with a distance Δx, the intersection of a line connecting the point of light source and point P with the grating plate is changed from G to G′ with a distance Δx_g as shown in Eq. 3.4,

$$\Delta x_g = \frac{z_p - z_g}{z_p - z_s}\Delta x. \tag{3.4}$$

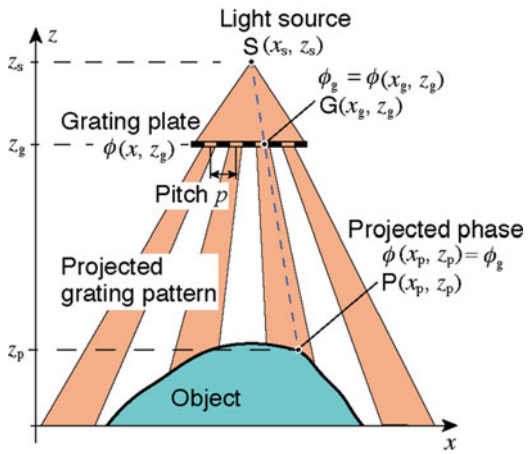

Fig. 3.1 Projected grating pattern with a point light source and a grating plate

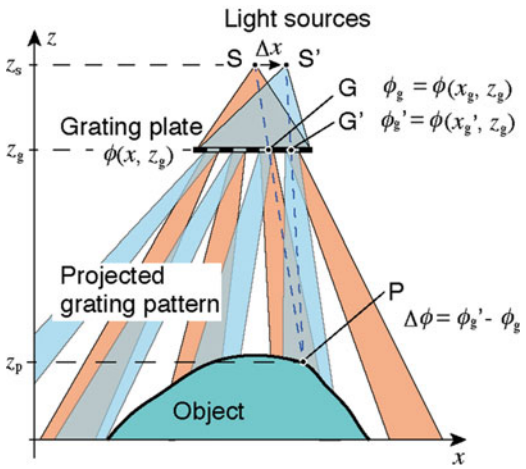

Fig. 3.2 Phase-shifted projected grating pattern using a light source stepping method

The projected phase at point P is shifted with $\Delta\phi$ as shown in Eq. 3.5,

$$\Delta\phi = \frac{2\pi}{p} \cdot \frac{z_p - z_g}{z_p - z_s} \Delta x. \tag{3.5}$$

This equation means that the projected phase is shifted in proportion as the light source stepping distance Δx and the proportionality coefficient is determined by the grating pitch of the grating plate and z positions of the light sources, grating plate and point P on the object. As the grating pitch of the grating plate, z position of the light sources and z position of the grating plate are fixed, the proportionality coefficient is corresponding to the z position of the object surface.

Actually, the light source is not a point but it has spatially spread. The light diffracts at the grating plate. So, the projected phase is exactly different from the right side of Eq. 3.3. However, when the grating pitch is around 1 mm, the influence of the diffraction is so small that the difference from Eq. 3.3 is small.

3.2.2 Whole-Space Tabulation Method (WSTM)

In the LSSM, shifted phase varies according to the z position as mentioned above. As the z coordinate and the obtained phase using an algorithm of a phase-shifting method have a one-to-one relationship.

We proposed a calibration method for an accurate and high-speed shape measurement using multiple reference planes. Figure 3.3 shows the principle of the calibration method. The reference plane oriented vertically to the z-direction is translated in the z-direction by small amount. A camera and a projector are arranged and fixed above the reference plane. The grating is projected from the projector onto the reference planes. The phase of the projected grating can be easily obtained using the phase-shifting method. A pixel of the camera takes an image on the ray line L in Fig. 3.3a. The pixel contains images of the points $P_0, P_1, P_2 \ldots P_N$ on the reference planes $R_0, R_1, R_2 \ldots R_N$, respectively. At each point, the grating phases $\theta_0, \theta_1, \theta_2 \ldots \theta_N$ can be calculated by the phase-shifting method. Therefore, the correspondence between the heights $z_0, z_1, z_2 \ldots z_N$ and the phases $\theta_0, \theta_1, \theta_2 \ldots \theta_N$, respectively, is obtained. From these phase-shifted images, the calibration tables are formed to obtain the z coordinate from the phase θ at each pixel as shown in Fig. 3.3b.

This method excludes a lens distortion and the intensity warping of the projected grating from measurement results theoretically. Tabulation makes short-time measurement possible because the z coordinate can be obtained by looking at the calibration tables from the phase at each pixel point and it does not require any time-consuming complex calculation.

3.3 Experiment

3.3.1 Experimental Setup

Figure 3.4a shows a photograph of a linear LED array device. There are nine parallel lines with 0.5 mm pitch. Each line has 30 LED chips connected in series. The size of a chip is a square of 350 μm by 350 μm. In Fig. 3.4a, the first left line is switched on and the other lines are switched off. Figure 3.4b shows a driver circuit for the linear LED array. Each line has a transistor (Toshiba, 2SC2240) as a switching device.

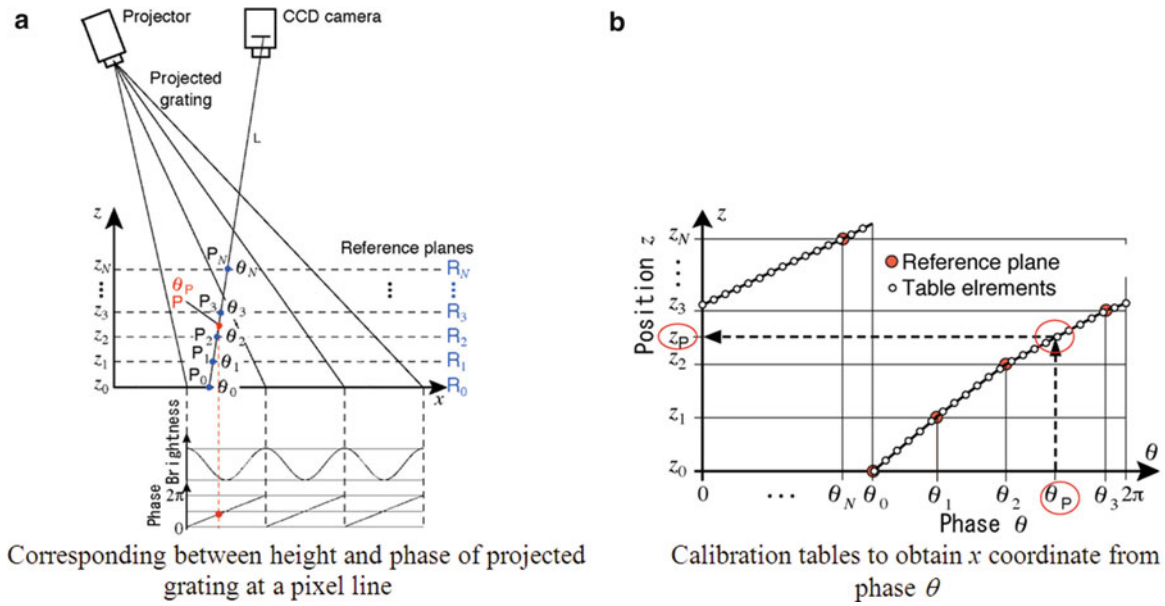

Fig. 3.3 Principle of whole-space tabulation method (**a**) Corresponding between height and phase of projected grating at a pixel line (**b**) Calibration tables to obtain x coordinate from phase θ

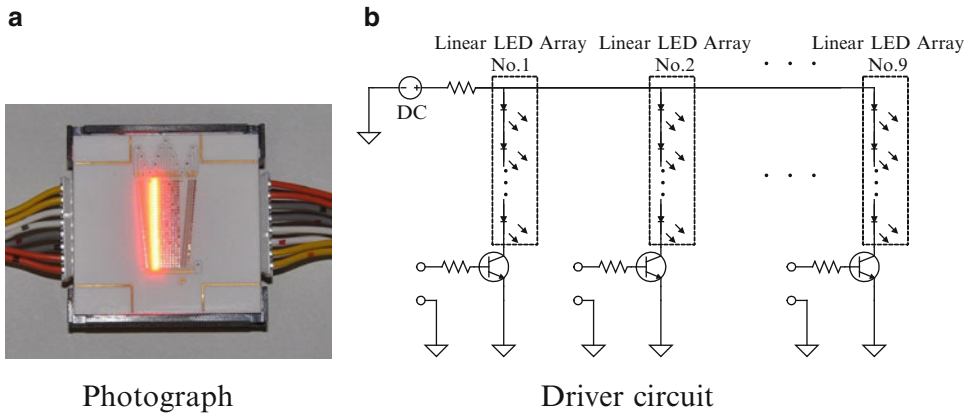

Fig. 3.4 Linear LED array device

Figure 3.5a shows a block diagram of an experimental setup. A high-speed camera (Redlake, Motion Xtra HG-100 K) is used. The orientation angle of the projector composed of the linear LED array device, a grating plate and a lens from the axis of the high-speed camera is 35°. The distance between the linear LED array device and the grating plate is 25 mm. The pitch of the grating plate is 1.02 mm. The distance between the grating plate and a lens is 15 mm. The projected grating pitch on the object can be reduced into 2.8 mm by this lens. It is necessary to increase the brightness to capture image in high speed. The measuring range is 4.0 mm in this case. A reference plane is translated from 0 to 5.0 mm at every 0.1 mm. The relationship between the phases of the projected gratin onto the reference plane and the z position was recorded to produce the phase-height tables for the WSTM. The calibration tables were produced at every $2\pi/1{,}000$ in phase.

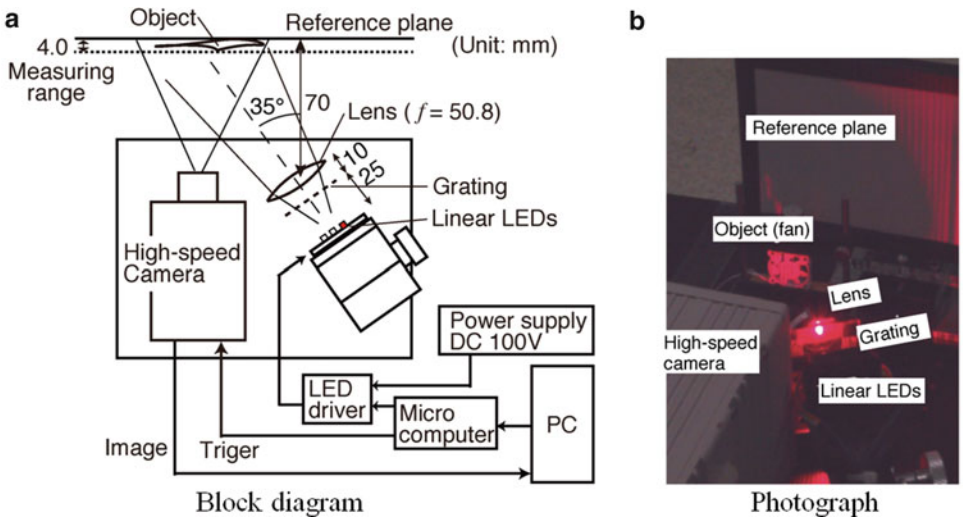

Fig. 3.5 Experimental setup

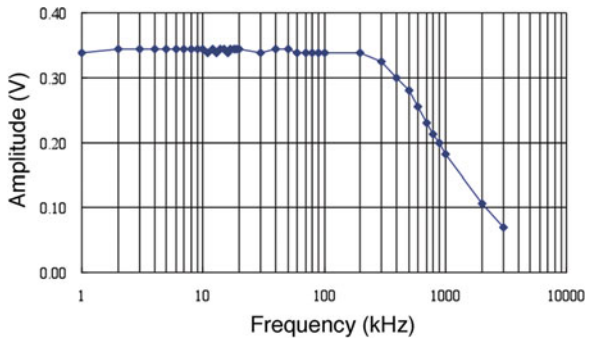

Fig. 3.6 Amplitude characteristic with changing the frequency of a rectangular wave from 1 to 3,000 kHz

3.3.2 Verification of Response Speed of Linear LED Array

Verification of the response speed of a linear LED array is performed. A pulse generator produces a square wave and it is applied to the base electrode of a transistor used as a switching device as shown in Fig. 3.5b. The voltage of power supply was 117 V and the lighting current is 113 mA. The response speed of a photo sensor and the amplifier is 100 MHz. The change of lighting power of the linear LED array is detected by the photo sensor. The amplitude of the input square wave and output wave is recorded by an oscilloscope simultaneously in time series. The frequency of input square wave is changed from 1 to 3 MHz.

The result of response speed of linear LED array is shown in Fig. 3.6. The output amplitudes of the photo sensor are almost same from 1 to 200 kHz. The output amplitude of the photo sensor in 1 MHz becomes half of the output amplitude in 200 kHz. This result shows that the linear LED array has enough ability to be applied for a high-speed shape measurement.

3.3.3 Experimental Results

A fan rotating with 29 times per second is used as an object. The phase shifting speed is 12,000 Hz. The grating images are grabbed by the high-speed camera synchronized with the phase shifting. Figure 3.7a shows a grating image projected onto the rotating fan. A phase shifting with three steps is performed in this experiment. The phase map of three phase shifted

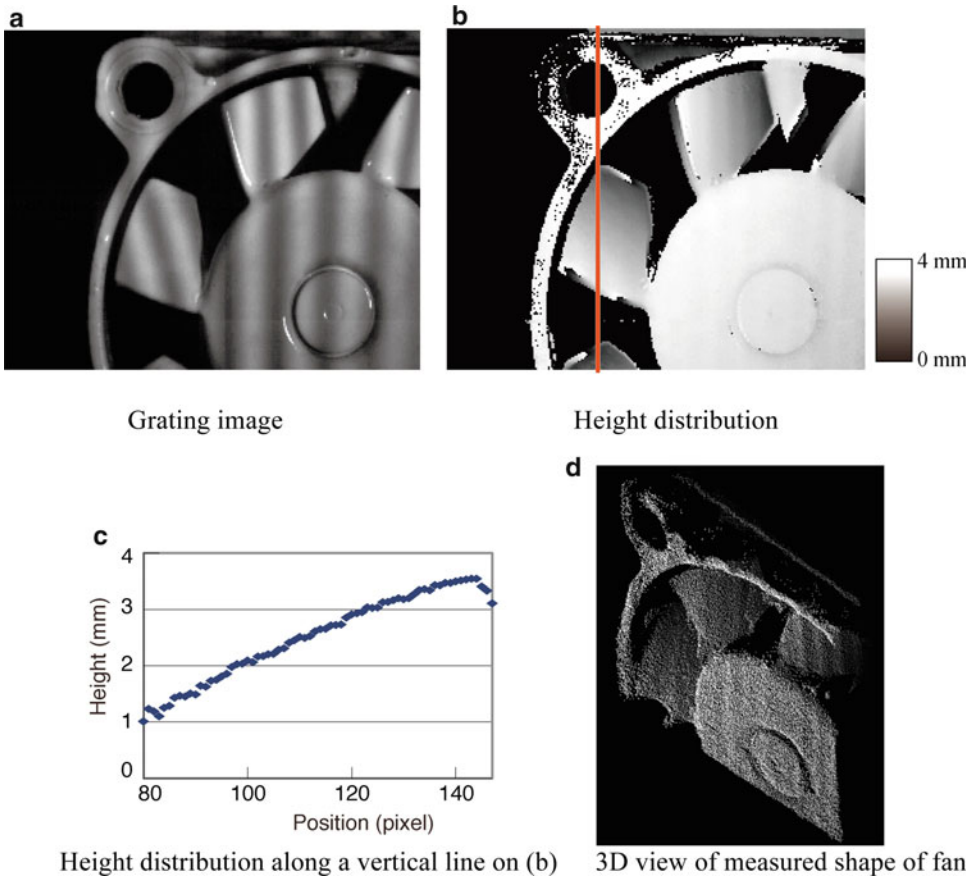

Fig. 3.7 Measured result of a rotating fan (**a**) Grating image (**b**) Height distribution (**c**) Height distribution along a vertical line on (**b**) (**d**) 3D view of measured shape of fan

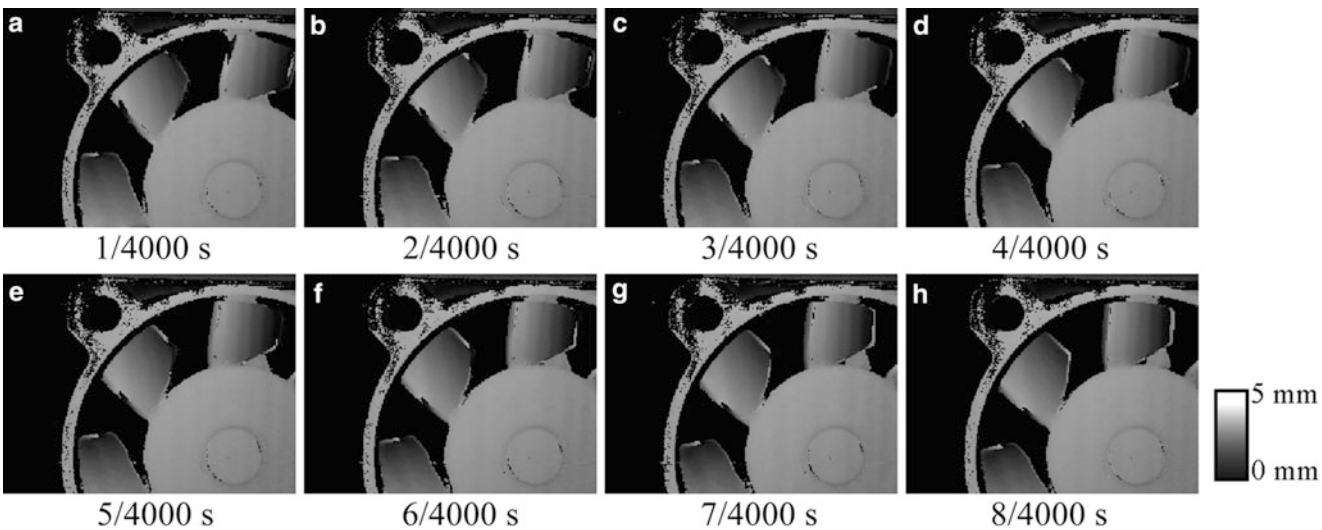

Fig. 3.8 Measured height distributions of a rotating fan in time series (**a**) 1/4,000 s (**b**) 2/4,000 s (**c**) 3/4,000 s (**d**) 4/4,000 s (**e**) 5/4,000 s (**f**) 6/4,000 s (**g**) 7/4,000 s (**h**) 8/4,000 s

grating images is obtained in every 1/4,000 s. The height distribution also obtained in every 1/4,000 s. Figure 3.7b shows a height distribution measured by this experimental setup. The cross section of the height distribution along a vertical line on Fig. 3.7b is shown in Fig. 3.7c. Figure 3.7d shows a 3D view of measured shape of the fan. Figure 3.8 shows the measured height distributions of a rotating fan in time series at intervals of 1/4,000 s.

3.4 Conclusions

High-speed shape measurement with a phase-shift grating projection method using a high-speed camera was performed in this paper. The LSSM using a linear LED array was employed as a grating projection method. The WSTM was employed to analyze the height distribution from obtained phase distribution. The WSTM is suitable for the LSSM. It was experimentally verified that the response speed of the linear LED array produced by authors was more than 200 kHz. In this experiment, the phase-shifting projection was performed in 12,000 Hz and the shape measurement of a rotating fan was performed in 4,000 Hz with three-steps phase shifting method.

Acknowledgement This research was supported by Hyogo COE program.

References

1. Morimoto Y, Fujigaki M, Toda H (1999) Real-time shape measurement by integrated phase-shifting method. Proc SPIE 3744:118–125
2. Fujigaki M, Matsumoto S, Masaya A, Morimoto Y, Murata Y (2012) Development of shape measurement system using mirrors for metallic objects. J JSEM 2(Special Isssue):194–197
3. Yen HN, Tsai DM, Yang JY (2006) Full-field 3-D measurement of solder pastes using LCD-based phase shifting techniques. IEEE Trans Electron Pack Manuf 29–1:50–57
4. Chan CS, Asundi AK (1994) Phase-shifting digital projection system for surface profile measurement. Proc SPIE 2354:444–452
5. Huang PS, Zhang C, Chiang F-P (2003) High-speed 3-D shape measurement based on digital fringe projection. Opt Eng 42–1:163–168
6. Zhang S, Weide DVD, Oliver J (2010) Superfast phase-shifting method for 3-D shape measurement. Opt Express 18–9:9684–9689
7. Gong Y, Zhang S (2010) Ultrafast 3-D shape measurement with an off-the-shelf DLP projector. Opt Express 18–19:19743–19754
8. Yoshizawa T, Wakayama T, Takano H (2007) Application of a MEMS scanner to profile measurement. Proc SPIE 6762:67620B-1-5
9. Asai D, Miyagi T, Fujigaki M, Morimoto Y (2010) Application to bin-picking of shape measurement using whole-space tabulation method with MEMS scanner grating projector. J JSEM 10(Special Issue):186–191
10. Zwick S, Fessler R, Jegorov J, Notni G (2012) Resolution limitations for tailored picture-generating freeform surfaces. Opt Express 20–4:3642–3653
11. Oura Y, Fujigaki M, Masaya A, Morimoto Y (2011) Development of linear LED device for shape measurement by light source stepping method. Opt Meas Model Metrol 5:285–291
12. Morimoto Y, Masaya A, Fujigaki M, Asai D (2012) Shape measurement by phase-stepping method using multi-line LEDs. In: Md. Zahurul Haq (ed) Applied measurement systems, InTech, Chapter 7, pp 137–152, http://www.intechopen.com/books/applied-measurement-systems; http://cdn.intechweb.org/pdfs/29356.pdf
13. Horikawa Y (2010) Japanese unexamined patent application publication no 2002-286432
14. Fujigaki M, Morimoto Y (2008) Shape measurement with grating projection using whole-space tabulation method. J JSEM (Japanese) 8(4):92–98
15. Fujigaki M, Takagishi A, Matui T, Morimoto Y (2008) Development of real-time shape measurement system using whole-space tabulation method, SPIE international symposium. Proc SPIE 7066:706606

Chapter 4
Deconvolving Strain Maps Obtained with the Grid Method

M. Grédiac, F. Sur, C. Badulescu, and J.-D. Mathias

Abstract The use of various deconvolution techniques to enhance strain maps obtained with the grid method is addressed in this study. Since phase derivative maps obtained with this measurement technique can be approximated by their actual counterparts convolved by the envelope of the kernel used to extract phases and phase derivatives, non-blind restoration techniques can be used to perform deconvolution. Six deconvolution techniques are compared here in order to restore a synthetic phase derivative map. Obtained results are analyzed and discussed.

Keywords Deconvolution • Displacement • Grid method • Strain measurement • Metrological performance

4.1 Introduction

Full-field measurement techniques are now wide spread in the experimental mechanics community. One of the reasons is their ability to measure heterogeneous states of strain and to detect localized events that often occur in specimens under test. Assessing the metrological performances of full-field measurement techniques remains an open issue. Recent papers published in this field mainly deal with digital image correlation [1, 2] for instance. One of the problems is that these performances depend on various parameters whose individual contribution is generally difficult to estimate [3].

Another problem is the fact that metrological performances depend on two conflicting concepts: resolution and spatial resolution. The first one is defined here by the smallest strain or displacement that can be detected, the second one by the smallest distance between independent measurements. It is well known that the better resolution, the worst spatial resolution. In addition, displacement is generally the physical quantity which is provided by many techniques but strain is the physical quantity involved in constitutive equations of engineering materials, so it often needs to be calculated. Since displacement maps are generally noisy, they are smoothed before differentiation which is performed to obtain strain components [4]. In conclusion, the number of parameters influencing the metrological performance is significant. This leads to confused ideas on the actual metrological performances of full-field measurement techniques, especially when strain components are considered instead of displacements.

M. Grédiac (✉)
Institut Pascal, UMR CNRS 6602, Clermont Université, Université Blaise Pascal, BP 10448, Clermont-Ferrand 63000, France
e-mail: Michel.Grediac@univ-bpclermont.fr

F. Sur
Laboratoire Lorrain de Recherche en Informatique et ses Applications, UMR CNRS 7503, Université de Lorraine, CNRS, INRIA projet Magrit, Campus Scientifique, BP 239, Vandoeuvre-lès-Nancy, Cedex 54506, France

C. Badulescu
Laboratoire Brestois de Mécanique et des Systèmes, ENSTA Bretagne, 2 rue François Verny, Brest, Cedex 9 29806, France

J.-D. Mathias
Laboratoire d'Ingénierie pour les Systèmes Complexes, IRSTEA, Campus universitaire des Cézeaux, 24 avenue des Landais, BP50085, Aubière, Cedex 63172, France

H. Jin et al. (eds.), *Advancement of Optical Methods in Experimental Mechanics, Volume 3*,
Conference Proceedings of the Society for Experimental Mechanics Series,
DOI 10.1007/978-3-319-00768-7_4,